Journal of Polymer Science and Engineering 2024, 7(1), 4070.
https://doi.org/10.24294/jpse.v7i1.4070

Article

Underwater implosion behavior of 3D-printed polymer structures

Nathan Grantham-Coogan[1], **Craig Tilton**[2], **Helio Matos**[1,*], **Arun Shukla**[1]

[1] University of Rhode Island, Kingston, RI 02881, USA
[2] Naval Undersea Warfare Center (Division Newport), Newport, RI 02841, USA
*** Corresponding author:** Helio Matos, hmatos@uri.edu

CITATION

Grantham-Coogan N, Tilton C, Matos H, Shukla A. Underwater implosion behavior of 3D-printed polymer structures. Journal of Polymer Science and Engineering. 2024; 7(1): 4070. https://doi.org/10.24294/jpse.v7i1.4070

ARTICLE INFO

Received: 6 January 2024
Accepted: 4 February 2024
Available online: 5 March 2024

Abstract: This study experimentally investigates the failure behavior of 3D-printed polymer tubes during underwater implosion. Implosion is a prevalent failure mechanism in the underwater domain, and the adaptation of new technology, such as 3D printing, allows for the rapid manufacturing of pressure vessels with complex geometries. This study analyzes the failure performance of 3D-printed polymer structures to aid in the future development of 3D-printed pressure vessels. The 3D-printed tube specimens analyzed were fabricated using digital light synthesis (DLS) technology and included four different case geometries. The geometries consist of three cylindrical shells of varying diameter and thickness and one double hull structure with a cylindrical gyroid core filler. These specimens were submerged in a pressure vessel and subjected to increasing hydrostatic pressure until implosion failure occurred. High-speed photography and Digital Image Correlation (DIC) were employed to capture the collapse event and obtain full-field displacements. Local dynamic pressure histories during failure were recorded using piezoelectric transducers. The findings highlight that the 3D-printed polymers underwent significant deformation and failed at localized points due to material failure. The fracture of the specimens during failure introduced inconsistencies in pressure and impulse data due to the chaotic nature of the failure. Notably, the energy flow analysis revealed that the proportion of energy released via the pressure pulse was lower than in traditional aluminum structures. These findings contribute to our understanding of the behavior of 3D-printed polymers under hydrostatic pressure conditions.

Keywords: 3D printed polymers; structural failure; implosion; cylindrical shells; double hull structures

1. Introduction

Undersea structures, such as unmanned underwater vehicles (UUVs) and underwater pipelines, are susceptible to failure when exposed to high hydrostatic pressure at greater operational depths. These failures can occur due to pressures exceeding their critical failure limit or dynamic loads from events in their immediate surroundings. To enhance the safety and efficiency of undersea operations, exploring innovative technologies capable of designing more robust underwater structures is crucial. One such technology is 3D printing, which offers numerous advantages such as design flexibility, customization, lightweight construction, simplified assembly, cost and time efficiency, and on-site production and repair capabilities [1]. By leveraging these benefits, 3D printing has the potential to revolutionize certain aspects of underwater operations by delivering improved performance, enhanced reliability, and cost-effectiveness. To aid in this development, this work analyzes the failure mechanisms of 3D-printed structures within a high-pressure underwater environment.

Extensive research has been conducted on hydrostatically induced failures over the past century. The implosion of objects emits pressure waves that can damage nearby structures [2,3], making implosion a subject of intense study. Early studies focused on the implosion of glass spheres [2–4], while NASA demonstrated interest in implosion studies for space vehicles [5]. More recently, there has been significant research on the implosion of cylindrical shells [6–8]. Researchers like Turner and Ambrico have characterized the pressure pulse of cylindrical metallic structures and developed accurate numerical models of the implosion process [6]. Additionally, composite materials have gained interest for their collapse mechanism, critical collapse pressure, and energy emitted during the implosion process [7,9,10].

Researchers have recently explored double-hull structures to enhance structural efficiency and mitigate energy during implosion events. However, most studies on cylindrical double-hull structures have focused on their performance under blast loading rather than hydrostatic loading [9,11,12]. While the study by DeNardo et al. examined hydrostatically induced failure in composite structures with foam as the filler material between the two shells [9], no research has been conducted on double hull structures with seamlessly connected shells and filler material. Li et al. investigated double hull structures using auxetics as the filler material and employed a numerical approach to study their post-buckling behavior [13].

This study aims to investigate the failure of 3D-printed double-hull structures by exploiting a 3D printer’s capability to produce advanced structures, which have not been explored in the literature. The investigation involves four specimens, including three cylindrical tubes and one double-hull structure. These specimens were subjected to increasing hydrostatic pressure until failure occurred, and their behavior was observed using high-speed cameras, Digital Image Correlation (DIC) analysis, and dynamic pressure sensors. The resulting data provided insights into the implosion characteristics of the material and enabled the calculation of the energy released during the implosion event. Furthermore, these experimental results were compared to numerical models created in Abaqus for specimen design.

2. Experimental procedures

2.1. 3D printing material

The specimens utilized in this study were produced using a carbon M2 resin printer. This printer has a build volume of 7.4 × 4.6 × 12.8 inches and can produce parts with relatively isotropic properties. The printing process involved using urethane methacrylate resin (UMA 90). A summary of the cured resin properties is presented in **Table 1** below.

Table 1. Material properties of UMA 90 are provided by carbon.

Property	**Value**
Elastic modulus	1400 MPa (~200,000 psi)
Poisson’s ratio	0.4
Yield stress	30 MPa (~4350 psi)

To ensure consistent quality, each UMA 90 part undergoes a post-processing procedure in accordance with the instructions provided in Carbon's technical sheet [14]. This procedure includes an IPA bath to remove excess resin, followed by one minute of UV light exposure on each side of the specimen using an APM LED UV-Cube-II.

2.2. Structural system

Four different specimen structures were considered in this study. The first three structures consist of cylindrical shell tubes with varying diameters and thicknesses. The fourth structure is a double hull design that combines two shells from the previous cases. The unsupported length of the tube structures is 25.4 cm in all cases. To prevent water penetration, each tube system is equipped with endcaps that seal its air interior from the underwater environment. The end caps are machined from aluminum 6061-T6 to have a snug fit to the inner tube surface and a 20 mm overlap with the tube's inner surface. In addition, an O-ring seal is placed between the end cap and the tuber's inner surface to prevent leakage during pressurization. **Figure 1** provides a visual representation of the longitudinal cross-sectional view of the four specimens, while **Table 2** presents the specific measurements of the first three cylindrical shell tubes.

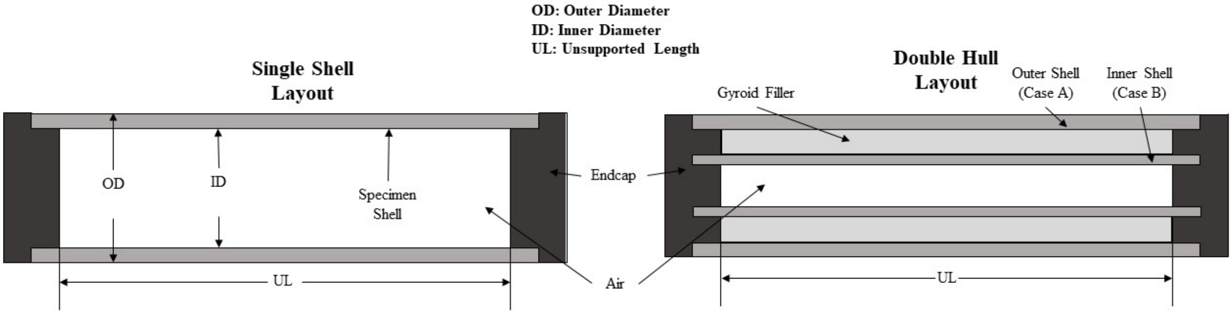

Figure 1. Specimen layouts for single shell and double hull specimens.

Table 2. Cylindrical shell specimen details.

Experimental designation	Structure type	Outer diameter (cm)	Inner diameter (cm)	Total thickness (cm)
Case A		5.08	4.45	0.32[a]
Case B	Single shell	2.54	2.23	0.16[a]
Case C		5.08	4.09	0.50[a]
Case D	Double hull	5.08	2.23	1.43[b]

a) The wall thickness of a single shell.
b) The wall thickness of two shells plus the core thickness.

The double hull structure is 3D printed as a single unit using a gyroid core filler, as illustrated in **Figure 1**. The gyroid shape was chosen because it is a common filler structure for 3D printing while highlighting the uniqueness of 3D printing to print complex geometries. To maintain the cylindrical shape, the gyroid structure was designed to bridge the outer and inner shells with a cell size of 1.27 cm (1/2 inch). The equation for a single gyroid unit shell in cartesian coordinates is represented in Equation (1).

$$0 = \cos(\omega x)\sin(\omega y) + \cos(\omega y)\sin(\omega z) + \cos(\omega z)\sin(\omega x) \quad (1)$$

In Equation (1), ω represents the gyroid unit cell's period, and x,y, and z represent the position in space in the cartesian coordinate system. To create the gyroid as a cylindrical shape, the gyroid is represented using polar coordinates. This transformation and mapping can be done similarly to a previous study by Wang et al. [15]. A MATLAB code that can recreate the cylindrical gyroid used in this study is in the Appendix and illustrated in **Figure A1** of the Appendix.

The unsupported length of the specimen, which measures 25.4 cm, was divided into twenty gyroid cells, resulting in a height of 1.27 cm for each cell. For the gyroid cylinder to connect properly, its circumference must consist of nine gyroid cells. Therefore, the circumference of each gyroid cell measured 1.33 cm (0.523 inches). The gyroid thickness, determined through the numerical model procedure, is 0.762 mm (0.03 inches). These dimensions and design considerations ensure the gyroid-filled double hull specimen's appropriate connection and structural integrity. Lastly, the thicker-walled cylindrical structure was designed for equivalent collapse pressure and displaced volume as the gyroid double hull structure.

2.3. Experimental setup

The experiments were conducted in the University of Rhode Island implosion tank facility. This facility comprises a semi-spherical pressure tank with a diameter of 2.1 m and is equipped with two high-speed cameras, as illustrated in **Figure 2**. The tank can handle pressures up to 6.9 MPa (1000 psi). During the experiments, the specimen was suspended in the center of the tank. The tank was then filled with water and pressurized using compressed nitrogen gas. To record the emitted signatures, three to four PCB 138A05 dynamic pressure transducers manufactured by PCB Piezotronics, Inc. (Depew, NY) were used to record pressure data at 2 MHz.

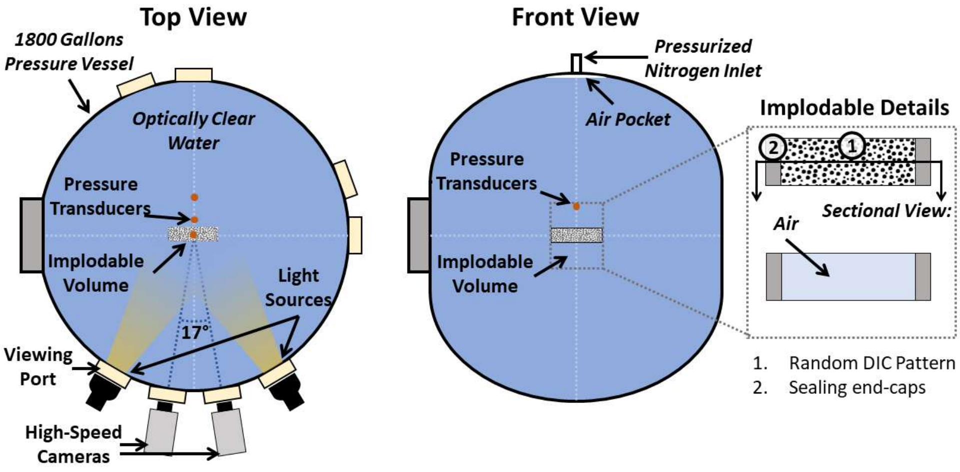

Figure 2. URI's implosion tank facility schematic.

The placement of the pressure sensors was determined to capture the implosion behavior and pressure signatures of each specimen, considering their respective outer diameters and dimensions. The schematic for the sensor locations is displayed in **Figure 3**.

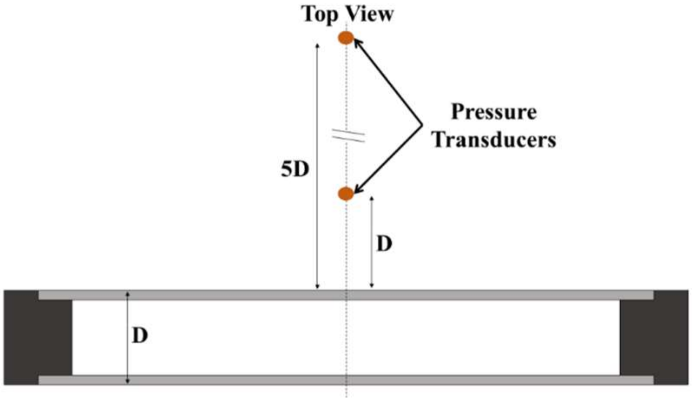

Figure 3. Sensor locations inside pressure tank.

2.4. Digital image correlation

High-speed cameras captured the implosion process at 40,000 frames per second. Each specimen was coated with a random DIC (Digital Image Correlation) pattern to facilitate accurate measurements of deformation. The speckle was high-contrast and randomized using a white UMA base and a random black speckle pattern using flat black paint.

Commercially available VIC-3D 9 software from Correlated Solutions, Inc. (Columbia, SC) was used for image analysis. The software enabled the extraction of out-of-plane displacements by comparing common pixel subsets between original undeformed and subsequent deformed images. Before usage, the system was calibrated using a 12 × 9 dots calibration grid with 18 mm spacing and periodically captured calibration grid images while translating and rotating the grid in all six degrees of freedom. This procedure is outlined in previous work [16–18]. Before pressuring the implosion tank at the beginning of the experiments, the calibration was validated by calculating the outer radius of the submerged cylinder using DIC (yielding errors of 5% or less). This validation procedure is also shown in previous work in more detail [19].

2.5. Post-processing calculations

2.5.1. Normalizing results

The results were normalized using the Buckingham-Pi theorem to facilitate effective comparison between all the cases. This normalization approach was initially made for energetic systems by the seminal work of GI Taylor [20]. It is now being adapted to the normalized pressure (π_p), in which the pressure (P) is multiplied by the cube of the sensor distance from the center of the implodable (R_s) and divided by the energy in the system (E_o), given by Equation (2). This value results in a dimensionless representation of the pressure energy relative to the initial energy of the implodable. Since sensor locations and initial energy vary between cases, this normalization is an important tool to assess the relative change between the cases. In addition, the initial potential energy in the implodable system was determined by multiplying the critical collapse pressure (P_{cr}) by the collapsible volume of the implodable (V_c), given by Equation (3).

$$\pi_P = \frac{PR_s^3}{E_o} \tag{2}$$

$$E_o = P_{cr}V_c \tag{3}$$

Similarly, the time history (t) was also normalized using the critical collapse pressure (P_{cr}), the collapsible volume (V_c), and the density of water (ρ_o), as given by Equation (4). The normalized time, π_p, represents the time it takes for the pressure wave generated by the implosion event to move in a particular medium relative to the size of the implodable (which affects how long the pressure wave is) and the initial pressure (which affects collapse velocity).

$$\pi_t = tP_{cr}^{\frac{1}{2}}V_{cr}^{-\frac{1}{3}}\rho_o^{-\frac{1}{2}} \tag{4}$$

2.5.2. Energy flux potential

To assess the damage potential of a failing implodable structure, the energy emission is calculated using the pressure signatures from the pressure transducers. Previous studies on implosion energy [10,21] performed these calculations by assuming a spherical pressure pulse to calculate energy flow. A spherical pulse is the general solution for a point source pressure pulse. However, a point source pulse is not a good assumption for the cases in this study when accounting for the tube geometry relative to the sensor location. In this work, an elliptical pressure wave surface is used to accommodate the cylindrical shape of the implodable. The ellipsoidal surface, *SA*, is calculated using the unsupported length of the implodable structure, *UL*, and the sensor location relative to the center of the implodable, *Rs*, as its major axis, given by Equation (5).

$$SA = 4\pi\left(\frac{2\left(\frac{UL}{2}R_s\right)^{1.6} + (R_s^2)^{1.6}}{3}\right)^{\frac{1}{1.6}} \tag{5}$$

To determine the maximum potential energy flux at the sensor location, E_{pf}, at the specific location, the potential energy in the system is divided by the surface area, as given by Equation (6). Note that E_o is a relatively high estimate for the actual energy release because (1) the pressure decreases during the collapse process, and (2) not the entire internal volume collapses during an implosion [10]. Previous work [10] accounted for the pressure decrease by calculating E_o as $\frac{1}{2}P_{cr}V^*$, where the ½ term accounts for the pressure drop and V^* is the collapsible volume of an assumed collapsed shape. However, the pressure is also not uniform throughout the wavefront surface area, close to the implosion event. Hence, SA is also a relatively high estimate for surface area if used with a point pressure measurement. Since E_o and SA are both overestimated, these overestimation factors will partially cancel out the calculation for the potential energy flux at the sensor location, E_{pf}.

$$E_{pf} = \frac{E_o}{SA} \tag{6}$$

2.5.3. Impulse and energy flux

The specific dynamic impulse, *I*, of the pressure generated during the implosion event, is calculated as the integral of the dynamic pressure signature, given by Equation (7), where t_i is the time in which the implosion initiates, and t_f is the time in which the low-pressure signatures of the implosion end (and the high-pressure starts).

$$I = \int_{t_i}^{t_f} (P - P_{cr}) dt \tag{7}$$

Lastly, earlier work on explosives by Aarons and Yennie [22] calculated the flow energy generated by an explosive bubble's collapse. Previous work [21] has leveraged these solutions by treating the implodable as a collapsible cavity. The energy flux generated by a collapsible cavity can be calculated using the impulse of the pressure signature, fluid properties, and measurement location as given by Equation (8).

$$E_f = \frac{I^2}{2\rho_o R_s} \tag{8}$$

Furthermore, the energy flux released can be normalized by dividing Equation (8) by Equation (6) to quantify the relative change in implosion pressure energy from different cases, providing valuable insights into the energy mitigation capabilities of the imploding structures.

As mentioned, the pressure is not uniform throughout the wavefront surface. Hence, Equation (8) gives a representative value that can be used to compare with other cases that use the same procedure to calculate E_f. A sensor array that can capture the pressure distribution would be needed for a better solution for total energy at the implosion wavefront. Another option is to use one sensor farther away from the implodable, in which case the point source spherical wavefront assumption becomes a valid option. The challenge with this latter option is having a sensor that has high sensitivity as well as having an implosion facility large enough to support a larger reflection-free window between t_i and t_f.

3. Preliminary analysis

3.1. Computational model

The double hull structure was a major design consideration when developing the implodable cases (Case D in **Table 2**). The inner and outer hulls are coupled through the core structure in the double hull structure. Unlike the single shell cases, where analytical tools such as the Von Mises buckling equation [23] can predict the collapse pressure, a computational model is required to design the implodable system for the desired collapse pressure given the displaced volume. Abaqus CAE 2022 was used to construct all the models, using the non-linear Riks solver to determine the collapse pressure.

3.1.1. Single shell

The material model used for the UMA 90 is given in **Table 1**, and the tube specimens were modeled using shells (for Cases A and B) and solid elements (for Case C). A unit pressure load was applied to the shell's exterior to simulate hydrostatic pressure. An equivalent force from the pressure around the endcaps was also applied to the ends of the tubes. Boundary conditions were implemented to model the endcaps, where the radial motion was fixed at the ends of the tube. The critical collapse pressure of the tubes was then determined by the maximum load proportionality factor (LPF) output. **Figures 4a** and **4b** illustrate the model for cases C and D, respectively, showcasing the boundary conditions and load application.

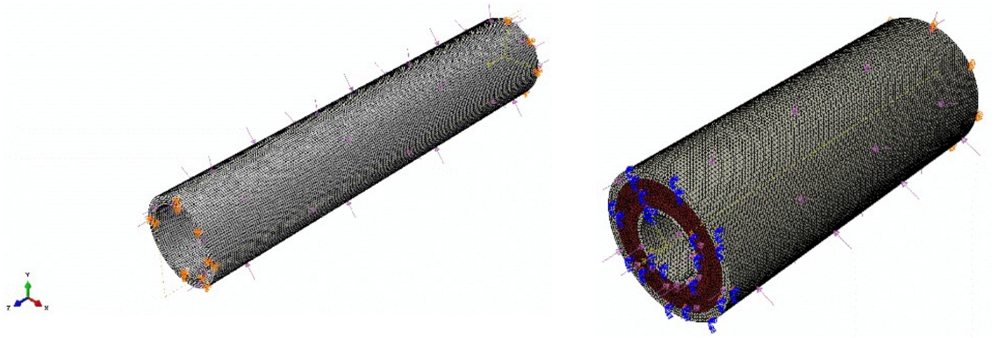
(a) **(b)**

Figure 4. (a) Single and **(b)** double hull tube structures model in Abaqus CAE.

3.1.2. Double hull structure

In Abaqus CAE, the double-hull structure was designed to maintain consistent boundary and loading conditions as in the single-shell simulations (as shown in **Figure 4a**). The gyroid core was also modeled using solid elements (shown in **Figure 4b** between the inner and outer shells as dark red). This is doable after simplifying the structural geometry and applying an effective bulk property to the double hull core.

Generally, single-shell simulations are relatively straightforward, but the double-hull structures were a challenge due to the structural complexities of the core. For complex structures, some validation tests representative of the mechanics should be made so the model can be calibrated to the validation test. Bending tests were performed for this work, as outlined in the following section. Another option would be to adopt a multiscale simulation approach, where the cores are simulated independently from the bulk structure (not used in this study).

3.1.3. Core properties

To determine the effective bulk property of the gyroid core structure, a series of 3 3-point bending (3PB) tests were performed in accordance with ASTM D5023. During these tests, sandwich beam structures with gyroid cores of the same cell size, periodicity, and total thickness as the double hull structure were performed with varying gyroid wall thickness. These tests were re-created using Abaqus CAE (as illustrated in **Figure 5**). Then, an iFEA approach was implemented to determine the effective elastic modulus for the given thickness to match the beam's flexural modulus (assuming Poison's core ratio is zero). **Table 3** summarizes the results for effective core properties as a function of gyroid thickness.

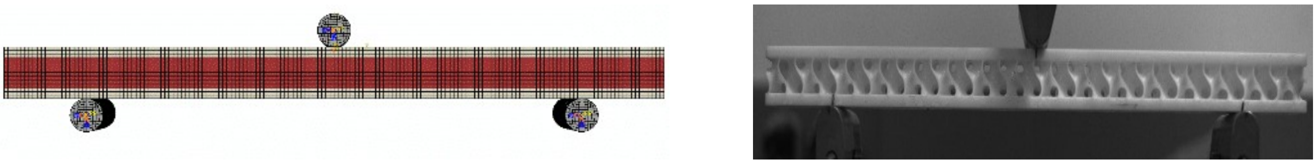
(a) **(b)**

Figure 5. 3 Point bending **(a)** Abaqus model layout **(b)** experimental setup.

Table 3. Effective core property.

Gyroid thickness (mm)	Effective elastic modulus in MPa
0.762	10.34
1.524	34.47
2.286	60.87
3.048	64.33

Lastly, a parametric study was performed using varying core elastic moduli, ranging from 10.34 to 64.33 MPa, to determine and estimate collapse pressure as a function of core wall thickness to determine the appropriate wall thickness that will yield a collapse pressure for the experimental facility (the facility limit is 6.9 MPa, but experiments were designed with a 75% cap on the limit for safety).

3.2. Computational design

After running Abaqus simulations of all cases and determining the appropriate wall thickness, the resulting collapse pressures for the designs are shown in **Table 4.**

Table 4. Specimen collapse pressures.

Experimental designation	Structure type	Computation design collapse pressure (MPa)	Experimental collapse pressure (MPa)	Prediction accuracy |Error|
Case A		0.7998	0.855	6.5%
Case B	Single shell	0.793	0.752	5.5%
Case C		3.792	4.551	16.7%
Case D	Double hull	3.758	4.029	7.2%

These results show errors ranging from 5 to 17% compared to the true collapse pressure observed in experiments. Different factors contribute to the prediction discrepancy of 3D printed structures. These factors should be considered when 3D printing structures with geometry and property sensitivity. These factors include the material residue after 3D printing, which can increase the overall thickness. Post-processing the part removes the residual for the most part, but post-processing is a very meticulous process. Also, when printing the different cases, even though they have the same height, the printing time was longer for the thicker shell, and the material was exposed to UV curing for longer. Hence, there can be a slight variation in mechanical properties in one-part thermoset materials, which are highly dependent on UV curing. Lastly, the print is being done from an STL file, which alters the circular shape into a polygon shape. Most CAD software (such as SolidWorks, which was used in this study) offers the option of a fine STL export, but a fine export is not on par with what is considered a fine mesh by FEA standards.

4. Results and discussion

4.1. Pressure results

In this study, the pressure data analysis focuses on the sensor located at one outer diameter of the specimen. It has been observed that as the collapse pressures decrease, this sensor registers higher spikes in pressure. As a result, the noise levels recorded by this sensor are lower than those located farther away from the specimen.

4.1.1. Cylindrical shells

This study's 3D-printed polymer material exhibits a different failure behavior than metal tubes or stronger materials. For metal tubes with relatively thin wall thickness, failure initiates due to the instability of the load relative to what the structure can support [7–10]. Instead of this instability failure, the failure initiates with plastic deformation of the specimen (before implosion—also referred to as pre-implosion deformation or pre-deformation), leading to imperfection and stress concentration on the lobes of the deformed tube. After reaching a critical stress, the implosion occurs after a crack propagates from the high-stress imperfections. These observations indicate that the implosion from these polymeric structures shows a material failure initiation, unlike traditional thin-walled structures, which fail with an instability initiation.

Figure 6 illustrates the implosion characteristics observed in the three shell tubes labeled based on their inner diameter. Critical instances during the implosion process are labeled in a sequence from A to E, from initiation to catastrophic implosion failure. The colormap overlayed on the tube's surface is the 3D DIC results for displacement, which show the change in radius relative to the center of the tube in millimeters. The corresponding pressure graphs for these trials are also presented with indicators A to E, showing what the structure looked like at these particular time instances. Each plot combines three trials, with the pressure data normalized by dividing it by the critical collapse pressure of each trial. For each plot, the average of all trials is shown as a solid line, and the sample standard deviation is given as the shaded area (this format is consistent for subsequent plots). The alignment of the pressure graph and accompanying photos is based on the implosion initiation, which sets the time to zero for each trial.

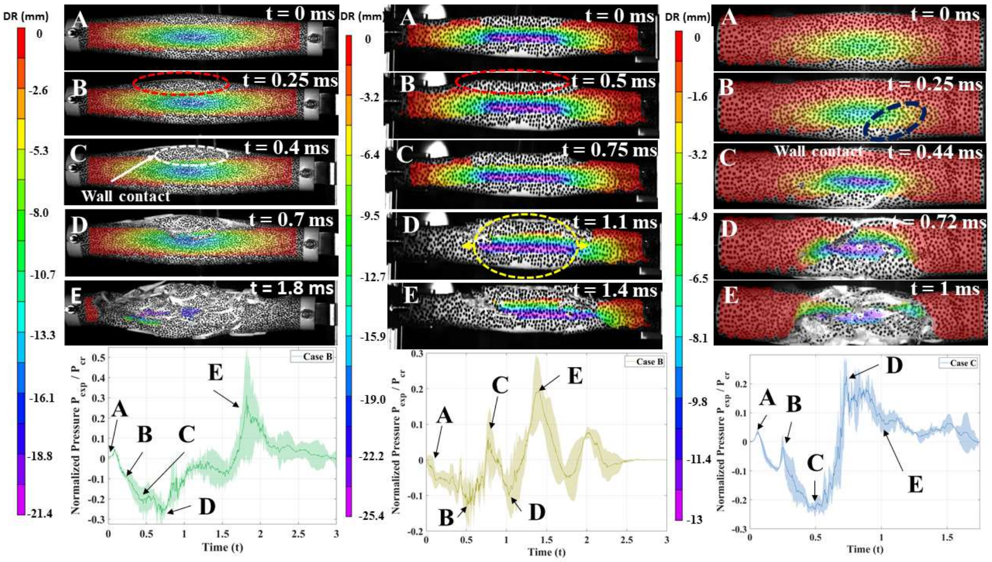

(a) (b) (c)

Figure 6. Normalized collapse pressure data for **(a)** Case A, **(b)** Case B, and **(c)** Case C.

The implosion initiates in time instance A, set to t = 0 in **Figure 6**. The first visible crack typically occurs along the top or bottom of the specimen and propagates longitudinally until it branches off and spreads throughout the specimen (B). This stage is characterized by major fracturing and increasing pressure variations between trials. The shell then undergoes implosion until wall contact occurs near the initial crack (C). At this point, the pressure pulse plateaus briefly as the rest of the specimen collapses. Subsequently, the specimen fractures into numerous pieces (D), and crack propagation continues until all the energy is released, resulting in the complete propagation of cracks (E).

Case C, which consists of the tube with a 4.089 cm (1.61 inch) inner diameter, exhibits a similar collapse behavior. Still, due to its thicker shell and higher collapse pressure, the pressure pulse data shows more consistency across different trials. Unlike Case A, which consists of a 4.45 cm inner diameter tube, a crack propagates during the implosion event along the center of the specimen (B) rather than the top or bottom. The collapse is also asymmetrical, with the side where the initial crack occurs experiencing a larger radial change than the other side, resulting in the walls not meeting in the middle.

The collapse characteristics of Case B, which is the tube with a 2.235 cm (0.88 inches) inner diameter, differ from those of the larger inner diameter tubes mentioned earlier. These tubes experience much greater deformation. The tube walls appear to be in contact even before the collapse is triggered (A). Failure begins with the formation of a crack at the top or bottom of the specimen, which propagates longitudinally (B). This is accompanied by a drop in pressure data and the formation and propagation of cracks throughout the specimen. At this stage, the walls in the center of the tube are completely in contact (C). Following the initial pressure spike, the rest of the specimen starts to collapse, resulting in additional spikes, as shown by D and E in **Figure 6c**.

The data were normalized using the Buckingham-Pi theorem to compare the results of all three trials. The normalized collapse pressure data for all three trials are presented in **Figure 7**. This normalization allows for a direct comparison of the collapse behavior and provides valuable insights into the implosion characteristics of the different tube specimens.

Among the three trials, the specimen with a 2.23 cm inner diameter (Case B) produced the lowest pressure pulse. This can be attributed to the high degree of deformation observed before the collapse in these experiments. With less distance for the walls to travel when instability occurs, the velocity of the shell walls is lower upon contact, resulting in a smaller pressure pulse.

In contrast, the inner diameters of the specimens at 4.09 cm (Case C) and 4.45 cm (Case A) exhibit significantly different characteristics in the under-pressure region during the collapse. This difference can be attributed to the fracture behavior observed in these trials, with the 4.09 cm specimen remaining more intact during the implosion event. Despite the variation in the under-pressure regions, the peak pressure pulse emitted from each experiment occurs at approximately the same location.

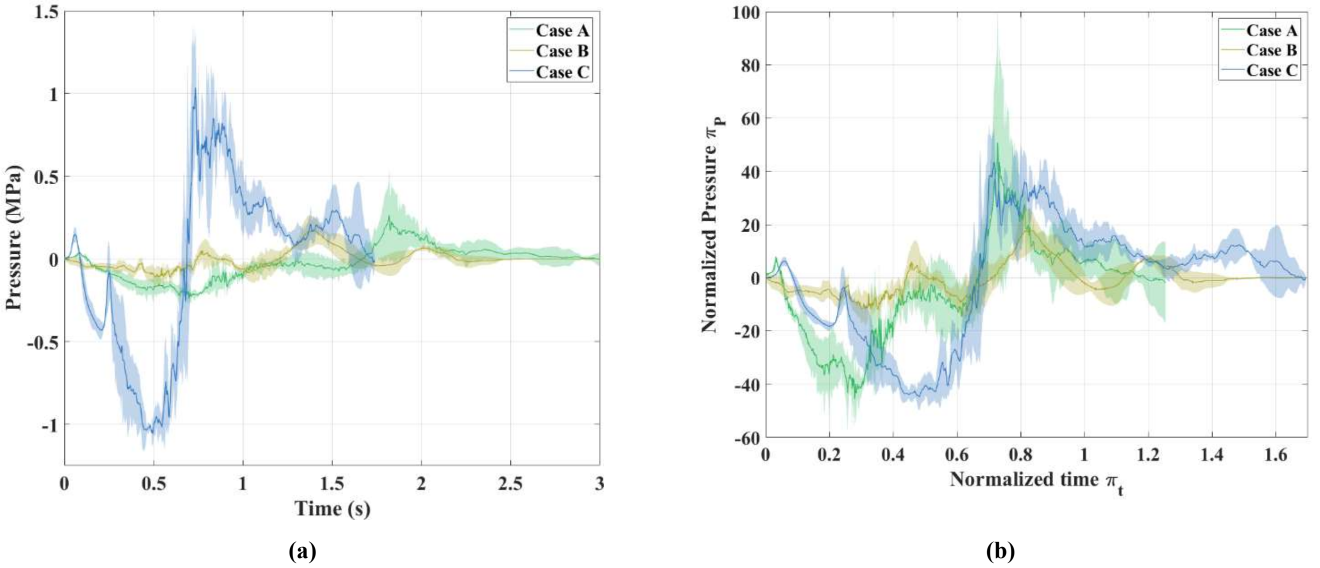

Figure 7. (a) Pressure vs. time for all cylindrical tubes **(b)** Normalized time vs. normalized pressure for all cylindrical tubes.

These variations in collapse characteristics among the three specimens highlight the complexity of predicting the exact outcome of a 3D-printed structure under hydrostatic pressure, especially when using a purely polymer structure. The additional complexities in failure mechanisms, coupled with the fact that polymers are inherently orders of magnitude weaker than metallics, make un-reinforced 3D printed polymer hull systems a unique choice for pressure hulls that may have a different application space (e.g., near-surface underwater vehicles with complex shapes that need rapid design and deployability). In addition, polymer parts of underwater structures are still necessary for non-structural applications in many undersea systems due to their lower impedance relative to metallics. Hence, these observations and findings are important in understanding the underwater structural behavior of 3D-printed polymer parts.

4.1.2. Double hull pressure data

The critical collapse pressure for the double hull, Case D, is 4.029 MPa with a standard deviation of 0.116 MPa. The collapse pressure shows a variation of 6%, which is relatively consistent compared to the shell tubes, which exhibited a percent error of 9%. This indicates a higher level of reliability and repeatability in the collapse behavior of the double-hull structure.

However, no notable data was recorded when analyzing the dynamic pressure sensors. This is due to the implosion behavior of this 3D-printed double-hull structure, driven by local failure (illustrated in the subsequent sections). This leads to water penetration at the local failure location and into the specimen. Water rushed inside the specimen, and a hammer occurred at the end cap locations. The pressure emitted from the local failure and internal hammer was negligible outside the specimen relative to the hydrostatic collapse pressure. For this reason, the collapse of this double-hull specimen cannot be accurately characterized using traditional cylindrical tube collapse analysis.

4.2. Displacement/DIC

4.2.1. Cylindrical shell displacement data

Table 5 presents the pre-deformation radius measurements obtained using DIC for the cylindrical shell specimens in different trials. The 3D DIC software directly measures the tube radius. The original radius, minimum radius before implosion is initiated (before any notable drop in hydrostatic pressure), and maximum radius percent change are provided for each trial. The measurements highlight the significant plastic deformation experienced by the specimens before failure, contributing to the variations in collapse pressure and failure characteristics.

Table 5. Cylindrical shell pre-deformation gathered using DIC.

Experiment	Original radius (cm)	Average minimum radius before implosion (cm)	Max radius percent change
Case A	5.54	0.957 ± 0.294	62.3 ± 11.6%
Case B	1.27	0.140 ± 0.139	89.0 ± 11.0%
Case C	2.54	1.62 ± 0.17	36.2 ± 6.8%

For case A, the radius change of 62.3% indicates a substantial shell deformation, leading to variations in collapse pressure and failure behavior among the trials. Similarly, case B undergoes significant deformation, with the walls almost touching before failure. The radius change of 89.0% indicates a high level of plastic deformation. In contrast, case C, the thicker shell specimen, exhibits comparatively lower deformation before failure.

These measurements highlight the influence of plastic deformation on the collapse behavior of the cylindrical shell specimens. The variations in deformation and collapse pressure among the trials can be attributed to factors such as fracture properties, plastic deformation properties, and material defects that may have been introduced during the 3D printing process. The observed pre-deformation provides insights into the complex nature of failure in these specimens and underscores the challenges of accurately predicting collapse behavior.

4.2.2. Double hull displacement data

Figure 8a illustrates the collapse process of the double hull structure. Before applying hydrostatic pressure, the structure is in its initial state. As the pressure increases, localized deformation occurs due to the presence of the gyroid structure providing structural support (0 ms). Once the critical point is reached, a crack forms at the point of maximum deformation, initiating the collapse (1 ms). The entry of water into the specimen causes significant damage to the affected region (2 ms). Unlike the shattered cylindrical shells, a significant portion of the double hull structure remains intact after the initial local failure.

In different trials, the initial failure points on the specimen vary. In **Figure 8b**, Trial 2 and Trial 3 specimens are shown before the collapse, with P0 representing the center point of the tube and P1 indicating the point of maximum deformation. In both trials, the failure initiates at the rear end of the specimen, which is not visible in the images. The presence of material imperfections is likely the primary factor contributing to the collapse of these specimens. As the hydrostatic pressure increases, these imperfections become more pronounced and lead to failure.

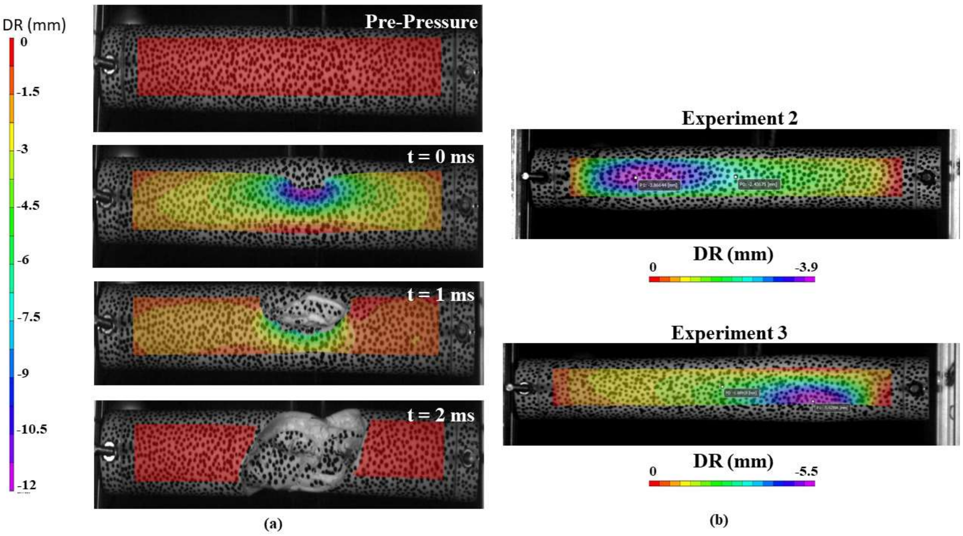

Figure 8. (a) Double hull structure collapse mechanism **(b)** Failure starting points for different experiments.

The average radius change before collapse for the double hull structure was 20.6%, with a standard deviation of 4.7%. As a result of localized failures, the specimens mostly remained intact during these trials. These observations demonstrate the influence of material imperfections and localized failure on the collapse behavior of the double hull structure. The variations in failure points and deformation patterns highlight the complex nature of collapse in these specimens and the challenges associated with predicting their behavior accurately. Interestingly, this type of implosion failure mechanism has little damage potential to its surroundings due to its low-pressure emissions.

4.3. Energy flow

Figure 9a illustrates the impulse behavior of the three single-shell tubes. The impulse values obtained from the experiments are used in Equation (8) to calculate the energy flux. The highest impulse value for each trial is selected to determine the energy flow, illustrated in **Figure 9b**.

Figure 10 presents the ratio of the maximum energy flow to the potential energy flux from Equation (6). This ratio represents the proportion of energy released through the pressure pulse. To facilitate comparison, the results from Pinto et al. have been adjusted to match the methodology described in this paper (using an elliptical area instead of the spherical area used in previous work [21]).

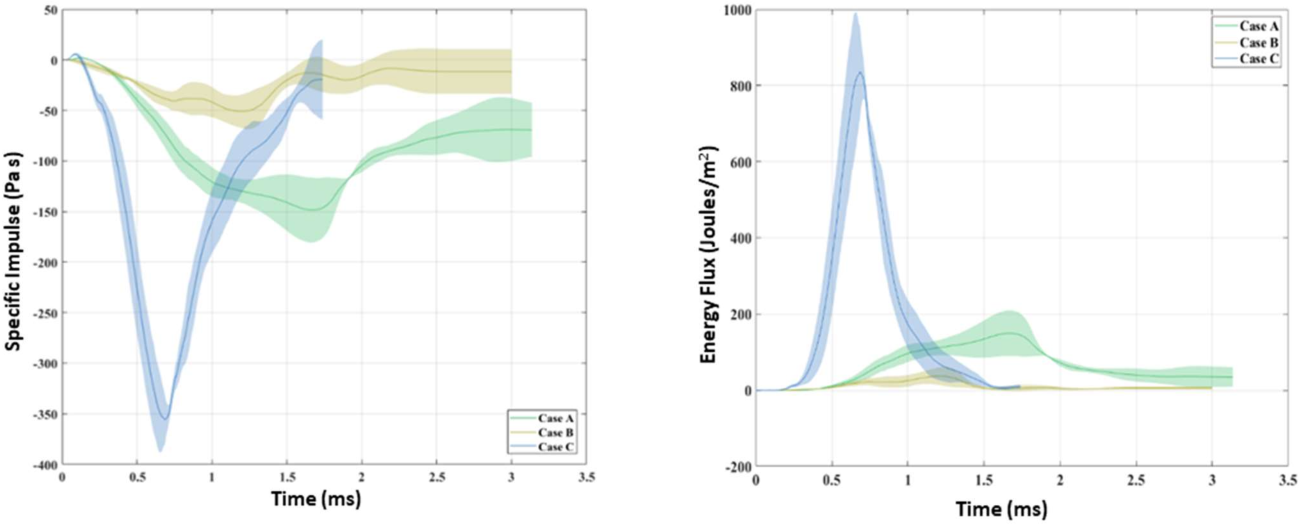

(a) (b)

Figure 9. (a) Impulse behavior of the three shell tubes **(b)** Energy behavior in Joules of the three shell tubes.

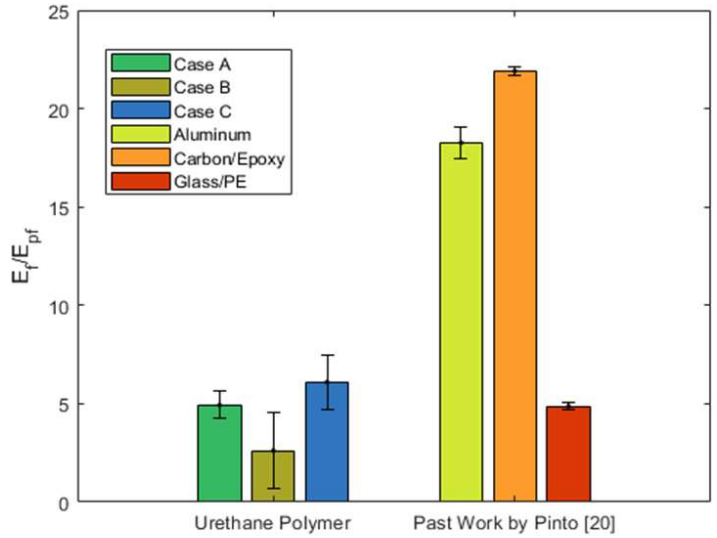

Figure 10. Flow energy as a percentage of the potential energy of each shell tube type compared with aluminum [21] results.

The results show that the polymer shell tubes exhibit lower energy flow than conventional aluminum tubes and carbon/epoxy specimens. It also shows comparable energy emissions to the Glass/PE specimens. The lower energy emission of Glass/PE tubes was attributed to the delamination/fracture damage induced during implosion. Similarly, the urethane polymer structures had a lot of fracture damage, which is energy-consuming. The polymer tubes also exhibit greater plastic deformation before implosion occurs. Among the shell tubes, the 2.23 cm inner diameter shell (Case B) displays the lowest energy flow to the potential energy average (as a variation), primarily due to the significantly higher pre-deformation observed in this specimen.

These findings highlight the unique behavior of the polymer shell tubes compared to other materials and provide insights into their energy dissipation characteristics during collapse. The differences in energy flow indicate the distinct failure mechanisms and deformation patterns exhibited by the polymer tubes, emphasizing the importance of considering the material properties and behavior when analyzing collapse phenomena.

5. Conclusion

This experimental investigation examined the behavior of 3D-printed polymer structures under critical hydrostatic pressure conditions. These structures' failure mechanisms and energy dissipation characteristics were analyzed using high-speed photography, the Digital Image Correlation (DIC) technique, and dynamic pressure sensors. The study yielded the following key conclusions:

1) Significant deformation occurs in the polymer tubes before failure, resulting in inconsistent critical collapse pressures. The variation in deformation contributes to the difficulty in accurately predicting the collapse behavior and emphasizes the importance of considering material properties and structural characteristics.
2) The fracture and deformation of the polymer material during implosion lead to lower energy flow emissions than traditional aluminum tubes. The unique properties of polymers result in a higher energy requirement for fracture and increased plastic deformation before implosion occurs.
3) The localized failure observed in double-hull structures is attributed to material imperfections. This type of implosion failure has negligible pressure signatures compared to its single hull equivalent system (Case C).

These findings provide valuable insights into the behavior of 3D-printed polymer structures under critical hydrostatic pressure. Understanding the failure mechanisms and energy dissipation characteristics is crucial for designing and engineering such structures and predicting their performance under extreme conditions.

Author contributions: Conceptualization, HM and AS; methodology, HM and AS; software, NGC; validation, NGC and HM; formal analysis, NGC and CT; investigation, NGC, HM and CT; resources, HM and AS; data curation, NGC; writing—original draft preparation, NGC and HM; writing—review and editing, NGC, CT, HM and AS; visualization, NGC; supervision, HM and AS; project administration, HM and AS; funding acquisition, HM and AS. All authors have read and agreed to the published version of the manuscript.

Data availability: The data that supports the findings of this study may be available upon request from the corresponding author. The data are not publicly available due to data control restrictions.

Disclaimer: The views expressed in this manuscript reflect the research results conducted by the author(s) and do not reflect the official policy or position of the Department of the Navy, Department of Defense, or the US Government. Some authors are US government employees, and this work was prepared as part of their official duties. Title 17 USC §105 provides that 'Copyright protection under this title is not available for any work of the United States Government.' Title 17 USC §101 defines US Government work as work prepared by a military Service member or employee of the US Government as part of their official duties.

Acknowledgments: The authors would like to acknowledge the support from the National Institute for Undersea Vehicle Technology (NIUVT), which provided the collaboration and financial means needed to complete this work.

Conflict of interest: The authors declare no conflict of interest.

References

1. Ngo TD, Kashani A, Imbalzano G, et al. Additive manufacturing (3D printing): A review of materials, methods, applications and challenges. Composites Part B: Engineering. 2018; 143: 172-196. doi: 10.1016/j.compositesb.2018.02.012
2. Urick RJ. Implosions as Sources of Underwater Sound. The Journal of the Acoustical Society of America. 1963; 35(12): 2026-2027. doi: 10.1121/1.1918898
3. Orr M, Schoenberg M. Acoustic signatures from deep water implosions of spherical cavities. The Journal of the Acoustical Society of America. 1976; 59(5): 1155-1159. doi: 10.1121/1.380977
4. Turner SE. Underwater implosion of glass spheres. The Journal of the Acoustical Society of America. 2007; 121(2): 844-852. doi: 10.1121/1.2404921
5. NASA space vehicle design criteria (structures). NASA SP-8007. NASA; 1968.
6. Turner SE, Ambrico JM. Underwater Implosion of Cylindrical Metal Tubes. Journal of Applied Mechanics. 2012; 80(1). doi: 10.1115/1.4006944
7. Farhat C, Wang KG, Main A, et al. Dynamic implosion of underwater cylindrical shells: Experiments and Computations. International Journal of Solids and Structures. 2013; 50(19): 2943-2961. doi: 10.1016/j.ijsolstr.2013.05.006
8. Gupta S, LeBlanc JM, Shukla A. Mechanics of the implosion of cylindrical shells in a confining tube. International Journal of Solids and Structures. 2014; 51(23-24): 3996-4014. doi: 10.1016/j.ijsolstr.2014.07.022
9. DeNardo N, Pinto M, Shukla A. Hydrostatic and shock-initiated instabilities in double-hull composite cylinders. Journal of the Mechanics and Physics of Solids. 2018; 120: 96-116. doi: 10.1016/j.jmps.2017.10.020
10. Matos H, Kishore S, Salazar C, et al. Buckling, vibration, and energy solutions for underwater composite cylinders. Composite Structures. 2020; 244: 112282. doi: 10.1016/j.compstruct.2020.112282
11. Huang S, Jin Z, Chen Y. Underwater blast resistance of double cylindrical shells with circular tube stiffeners. Ocean Engineering. 2021; 238: 109691. doi: 10.1016/j.oceaneng.2021.109691
12. Huang S, Tong X, Chen Y, et al. Effects of Internal Fluid on the Dynamic Behaviors of Double Cylindrical Shells Subjected to Underwater Explosion. Journal of Offshore Mechanics and Arctic Engineering. 2022; 144(4). doi: 10.1115/1.4053699
13. Li C, Yang J, Shen HS. Postbuckling of pressure-loaded auxetic sandwich cylindrical shells with FG-GRC facesheets and 3D double-V meta-lattice core. Thin-Walled Structures. 2022; 177: 109440. doi: 10.1016/j.tws.2022.109440
14. UMA 90 Technical Data Sheet. Carbon, Inc.; 2020.
15. Wang Y, Ren X, Chen Z, et al. Numerical and experimental studies on compressive behavior of Gyroid lattice cylindrical shells. Materials & Design. 2020; 186: 108340. doi: 10.1016/j.matdes.2019.108340
16. Gupta S, Parameswaran V, Sutton MA, et al. Study of dynamic underwater implosion mechanics using digital image correlation. Proceedings of the Royal Society A: Mathematical, Physical and Engineering Sciences. 2014; 470(2172): 20140576. doi: 10.1098/rspa.2014.0576
17. Gupta S, Matos H, Shukla A, et al. Pressure signature and evaluation of hammer pulses during underwater implosion in confining environments. The Journal of the Acoustical Society of America. 2016; 140(2): 1012-1022. doi: 10.1121/1.4960591
18. Matos H, Gupta S, Shukla A. Structural instability and water hammer signatures from shock-initiated implosions in confining environments. Mechanics of Materials. 2018; 116: 169-179. doi: 10.1016/j.mechmat.2016.12.004
19. Matos H, Shukla A. Mitigation of implosion energy from aluminum structures. International Journal of Solids and Structures. 2016; 100-101: 566-574. doi: 10.1016/j.ijsolstr.2016.09.030
20. Taylor GI. The formation of a blast wave by a very intense explosion I. Theoretical discussion. Proceedings of the Royal Society of London Series A Mathematical and Physical Sciences. 1950; 201(1065): 159-174. doi: 10.1098/rspa.1950.0049

21. Pinto M, Matos H, Gupta S, et al. Experimental Investigation on Underwater Buckling of Thin-Walled Composite and Metallic Structures. Journal of Pressure Vessel Technology. 2016; 138(6). doi: 10.1115/1.4032703
22. Arons AB, Yennie DR. Energy Partition in Underwater Explosion Phenomena. Reviews of Modern Physics. 1948; 20(3): 519-536. doi: 10.1103/revmodphys.20.519
23. Von Mises R, Windenburg DF. The critical external pressure of cylindrical tubes under uniform radial and axial load. Defense Technical Information Center; 1933. doi: 10.21236/ad0136219

Appendix

Core for double hull structure:

```
clear all; clc;

% Define resolution for the grid (complex number to specify the number of points)
res = 100j;
% Define lattice parameters
a = 1;
b = 1;
c = 1;

% Calculate reciprocal lattice parameters
kx = 2*pi / a;
ky = 2*pi / b;
kz = 2*pi / c;

% Create the grid in cylindrical coordinates
[r_aux, phi, z] = ndgrid(linspace(0, a, imag(res)), ...
                         linspace(0, b, imag(res)), ...
                         linspace(0, 20*c, imag(res)));

% Convert r_aux range to actual radii
r1 = 0.5;
r2 = 0.875;
r = (r2 / a) * r_aux + (r1 / a) * (1 - r_aux);

% Define the gyroid function
Gyroid = @(x, y, z) (cos(kx*x).*sin(ky*y) + ...
                     cos(ky*y).*sin(kz*z) + ...
                     cos(kz*z).*sin(kx*x));

% Compute data for the cylindrical gyroid
% r_aux is x, phi * 12 is y, and z is z
fun_values = Gyroid(r_aux, phi * 9, z);

% Compute Cartesian coordinates for grid points
x = r .* cos(phi * ky);
y = r .* sin(phi * ky);

% Create the structured grid
grid = struct('x', x(:), 'y', y(:), 'z', z(:), 'vol3', fun_values(:));

% Reshape the data for isosurface
num_points_per_axis = imag(res);
x_reshaped = reshape(x, num_points_per_axis, num_points_per_axis, num_points_per_axis);
y_reshaped = reshape(y, num_points_per_axis, num_points_per_axis, num_points_per_axis);
z_reshaped = reshape(z, num_points_per_axis, num_points_per_axis, num_points_per_axis);
fun_values_reshaped = reshape(fun_values, num_points_per_axis, num_points_per_axis, num_points_per_axis);

% Create an isosurface
iso_value = 0;
fv = isosurface(x_reshaped, y_reshaped, z_reshaped, fun_values_reshaped, iso_value);

% Extract the vertices and faces from the isosurface data
```

```
vertices = fv.vertices;
faces = fv.faces;

% Calculate colors based on the z-coordinate of vertices
colors = vertices(:, 3);

% Plot the cylindrical gyroid
fig = figure;
patch(‘Faces’, faces, ‘Vertices’, vertices, ...
    'FaceVertexCData', colors, 'FaceColor', 'interp', 'EdgeColor', 'none');
xlabel('X');
ylabel('Y');
zlabel('Z');
colormap jet;
colorbar;
axis equal;
grid on;
view(3);
```

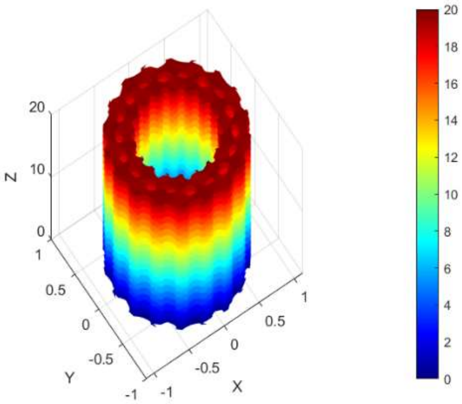

Figure A1. Gyroid core coordinates (in inches).